

Barometric pumping through fractured rock: a mechanism for venting deep methane to Mars' atmosphere

J. P. Ortiz^{1,2}, H. Rajaram², P. H. Stauffer¹, D. R. Harp^{1*}, R. C. Wiens^{3†}, K. W. Lewis⁴

¹Computational Earth Science, Los Alamos National Laboratory, Los Alamos, NM, USA

²Dept. of Environmental Health and Engineering, The Johns Hopkins University, Baltimore, MD, USA

³Space and Remote Sensing, Los Alamos National Laboratory, Los Alamos, NM, USA

⁴Dept. of Earth and Planetary Sciences, The Johns Hopkins University, Baltimore, MD, USA

Contents of this file

1. Minimum Depth of Living Microbes
2. Data Processing
3. Subsurface Flow and Transport Simulations
 - (i) Governing Equations and Boundary Conditions
4. Fracture Network
 - (i) Fracture Generation Algorithm
 - (ii) Upscaling of Properties
 - (iii) Fracture Network Topology
5. Correlation of Atmospheric Abundance Measurements and Surface Flux
 - (i) Cross-Correlation
 - (ii) Linear Correlation
6. Additional Results
7. Figures S1 to S18

* Current affiliation: Science and Analytics Team, The Freshwater Trust, Portland, OR, USA

† Current affiliation: Earth, Atmospheric, and Planetary Sciences, Purdue University, West Lafayette, IN, USA

1. Minimum Depth of Living Microbes

While methane sources may be either biotic or abiotic in origin, current production of methane by living organisms is most likely to be restricted to depths far below the regolith (uppermost soil) due to inhospitable surface conditions (Boston et al., 1992). Living methanogens could exist on Mars in endolithic habitats (i.e., within pore spaces) (Lollar et al., 2006; Lin et al., 2006) at temperatures between -20° and 122°C (Jones et al., 2011) provided there is some amount of liquid water or brines present. The likely minimum depth for living organisms in Mars’ crust has previously been reported as ~ 150 m (Mellon & Phillips, 2001) – a depth coincident with the melting isotherm of water at a latitude of 50° S – and has been used as the minimum baseline depth in more recent research regarding potential microbial activity (Tung et al., 2005) and habitable environments (Oehler & Etiope, 2017) on Mars. At more equatorial latitudes, such as Gale crater ($\sim 5^{\circ}$ S), the melting isotherm is shallower (~ 90 m), though liquid water is more likely to be stable at greater depths (≥ 200 m) when overlain by dry, unconsolidated regolith with low conductivity and geothermal heat flux (Mellon & Phillips, 2001). Orbiting radar suggests that large-scale brine bodies are not common at depths shallower than ~ 200 m (Stamenković, Ward, et al., 2019; Stamenković, Beegle, et al., 2019; Carrier et al., 2020). We therefore use 200 m as a conservative estimate for the minimum depth of extant methanogenic life, though this depth will vary from location to location across Mars due to the geothermal gradient, crustal conductivity, and heat flow (Tung et al., 2005), which are not precisely known. This depth is within the envelope of the martian biosphere phase model (depth, pressure, temperature) (Jones et al., 2011) that highlights the overlapping phase space of terrestrial life extrapolated to Mars’ subsurface environments. Evidence exists for such communities on Earth, in some locations at depths of 2-3 km (Lollar et al., 2006; Lin et al., 2006).

2. Data Processing

We drove our simulations using atmospheric pressure fluctuations from Gale Crater collected by *Curiosity* Rover Environmental Monitoring Station (MSL-REMS; <https://pds.nasa.gov/>) through mission sol 2713. The REMS contains all the weather instruments aboard *Curiosity* needed to provide information on the meteorological conditions around the rover. It measures and provides daily and seasonal reports on atmospheric pressure, humidity, wind speed/direction, ultraviolet radiation at ground surface, air temperature, and ground temperature around the rover. Atmospheric pressure is measured using a sensor inside the rover’s chassis that is connected to the external atmosphere via a tube that exits the rover body through a small opening. The MSL-REMS data contain a number of temporal data gaps due to instrument downtime and errors. Some of these data gaps span multiple diurnal periods, which could be problematic in our simulations where such signals are important. Below, we describe our approach to filling these gaps based on spectral analysis of the pressure record.

Our first step in processing was to perform an elevation-pressure correction due to change in *Curiosity* rover’s position in time. We gathered rover positional data (Figure S1), then calculated the relative pressure offset caused by elevation change using a simple air-static condition: $p(z) = p_0 + \rho_{air}gz$, where $p(z)$ is the adjusted air pressure [Pa], p_0 is the air pressure [Pa] at the landing site, ρ_{air} is approximate air density [kg m^{-3}] at the landing site, and z is the elevation [m] relative to the landing site.

We then performed an initial decomposition of the pressure data into the frequency domain using a Fast Fourier Transform (FFT) algorithm (Cooley & Tukey, 1965) to get a preliminary estimate of the dominant barometric components. In order to obtain a uniform measurement spacing, we interpolated over data gaps using a Piecewise Cubic Hermite Interpolating Polynomial (PCHIP). This method has an advantage over linear interpolation for periodic signals in that it better preserves the original shape of the data. This method meets the requirement for FFT in that it produces evenly-spaced data, but it is unable to interpolate the shape of the data over more than one period. This initial FFT revealed two significant high-frequency barometric components with periods 0.5 and 1.0 sols (semi-diurnal and diurnal fluctuations). Other significant barometric components exist, but the periods of such components were much longer (> 300 sols) than the longest gaps in the data (tens of sols), so they were ignored for the procedure described below.

We proceeded to fill the gaps > 0.5 sols in the unprocessed barometric record since this is the longest period the PCHIP method can be expected to successfully interpolate. We algorithmically selected windows around missing data, making sure to include multiple cycles of non-missing data on either side of the gap. Then, for each window, we calibrated a synthetic Fourier series to the non-missing data with which to fill the gap based on the data enveloping it. We used a two-component Fourier series with periods

0.5 and 1.0 sols (from the initial FFT) and calibrated the associated phase shifts and amplitudes (Figure S3). We then interpolated the data to 15-minute intervals using the PCHIP method. The resulting data are shown in Figure S4.

3. Subsurface Flow and Transport Simulations

The Finite Element Heat and Mass transfer code (FEHM; <https://fehm.lanl.gov/>), a multiphase flow and transport model developed at Los Alamos National Laboratory, was used for all numerical simulations. FEHM solves the conservation of mass and momentum equations using the finite volume method (Zyvoloski, 2007; Zyvoloski et al., 2021). The reader is referred to Fung, Hiebert, and Nghiem (1992) and Zyvoloski (2007) for more detail.

The major assumptions in the FEHM implementation of the flow model are those associated with Darcy’s law for fluid flow in porous media (Zyvoloski, 2007). This restricts fluid velocity to be relatively slow and laminar. This assumption is nearly always valid in porous media and fracture flow regimes. Another assumption is that the rock phase is rigid (i.e., non-deformable).

Although FEHM is capable of simulating multi-phase flow and transport, we have assumed single-phase air flow and vapor-phase transport in order to simplify the code modifications necessary to adapt FEHM to Mars conditions (e.g., reduced gravity, differing composition of carrier gas “air”, much lower temperatures). We note that the composition of air on Mars is $\sim 95\%$ CO₂ and is much thinner than that in Earth’s atmosphere; air density near the surface of Mars is close to the air density at an altitude of 30 km on Earth.

3.1. Governing Equations and Boundary Conditions

3.1.1. Flow

The governing flow equations for single-phase flow of a carrier gas (Mars air) in the fracture network are given by:

$$b \frac{\partial \rho}{\partial t} + \nabla \cdot (\rho \vec{Q}_f) = \sum (\rho \vec{q} \cdot \vec{n})_I, \text{ where} \quad (1)$$

$$\vec{Q}_f = -\frac{b^3}{12\mu} \nabla (P_f + \rho g z) = -\frac{bk_f}{\mu} \nabla (P_f + \rho g z) \quad (2)$$

where ∇ is the 2-D gradient operator (operating in the fracture plane), ρ is the air density [kg m^{-3}], t is time [s], \vec{Q}_f is the in-plane fracture flux [$\text{m}^2 \text{ s}^{-1}$], \vec{q} is the volumetric flux [$\text{m}^3/(\text{m}^2 \text{ s})$] of air in the rock matrix, \vec{n} denotes the normal at the fracture-matrix interfaces (I), b is the fracture aperture [m], μ is the dynamic viscosity of air [Pa s], P_f is air pressure within the fracture [Pa], k_f is fracture permeability [m^2], g is gravitational acceleration [m s^{-2}], and z is elevation [m]. The right-hand side of (1) represents the fluxes across the fracture-matrix interface. Note that (1) is an aperture-integrated two-dimensional equation for fracture flow and (2) is the local cubic law for laminar fracture flow (Zimmerman & Bodvarsson, 1996).

Governing equations for flow in the matrix are given by:

$$\phi \frac{\partial \rho}{\partial t} + \nabla \cdot (\rho \vec{q}) = 0, \text{ where} \quad (3)$$

$$\vec{q} = -\frac{k_m}{\mu} \nabla (P_m + \rho g z) \quad (4)$$

where ∇ is the 3-D gradient operator, ϕ is the porosity [$- ; \text{m}^3/\text{m}^3$], k_m is matrix permeability [m^2], P_m is the air pressure in the rock matrix [Pa]. Note that $P_f = P_m$ on the fracture-matrix interface (I), and the pressure gradients ∇P_m at the fracture-matrix interface control the right-hand side of (1). We make the assumption that the bulk movement of air through the rock matrix behaves according to Darcy’s law (4). In the case of a low-permeability rock matrix, the pressure gradients and fluxes induced in the matrix by barometric pressure variations are typically small.

3.1.2. Transport

The governing equations for transport of a tracer gas (e.g., methane) in a fracture are given by:

$$b \frac{\partial (\rho C_f)}{\partial t} + \nabla \cdot (\rho \vec{Q}_f C_f) - \nabla \cdot (b \rho D \nabla C_f) = \sum [(\rho \vec{q} C_m + \phi \rho D \nabla C_m) \cdot \vec{n}]_I + \dot{m}_f \quad (5)$$

where C_f/C_m is tracer concentration [$\text{mol kg}_{\text{air}}^{-1}$] in the fracture and matrix, respectively; D is the free-air molecular diffusion coefficient of the tracer [$\text{m}^2 \text{s}^{-1}$]; and \dot{m}_f is the tracer source in the fracture plane [$\text{mol m}^{-2} \text{s}^{-1}$]. The first term on the right-hand side of 5 represents the tracer mass fluxes across the fracture-matrix interfaces. Note that the mass fluxes across fracture-matrix interfaces include advective and diffusive fluxes. Even in the absence of significant air flow in the matrix, diffusive flux exchanges between the fracture and matrix persist and are included in our formulation. Governing equations for transport in the rock matrix are given by:

$$\phi \frac{\partial \rho C_m}{\partial t} + \nabla \cdot (\rho \bar{q} C_m) - \nabla \cdot (\phi \rho D \nabla C_m) = \dot{m}_m \quad (6)$$

where \dot{m}_m is the tracer source in the matrix [$\text{mol m}^{-3} \text{s}^{-1}$], and $C_f = C_m$ on the fracture-matrix interface.

The flow and transport equations are solved using the FEHM simulator, which employs computational approaches that are well established in the field of subsurface hydrogeology.

The no-flux boundary on the bottom of the domain is used to represent an impermeable bedrock or ice layer at depth (200 m). We did not find the proximity of the methane source (195 - 200 m depth) to this no-flux boundary to significantly affect simulation results. Moving the methane source away from the no-flux boundary (as in the shallow (150 m) case; Figure S14) resulted in greater surface flux – rather than less – due to being closer to the surface, which is the expected behavior.

4. Fracture Network

4.1. Fracture Generation Algorithm

The model is set up in FEHM as a two-dimensional planar domain 50 m wide by 200 m deep. The computational mesh was generated using the LANL developed software GRIDDER (<https://github.com/lanl/gridder>, 2018). Mesh discretization is uniform in the x and y directions such that $\Delta x = \Delta y = 1$ m. We randomly generated orthogonal discrete fractures using the 2-D Lévy-Lee algorithm (Clemo & Smith, 1997), a fractal-based fracture model (Geier et al., 1988). In this model, fracture centers are created sequentially by a “Lévy flight” process, a term coined by Benoît Mandelbrot and named for Paul Lévy in which the step lengths in a random walk follow the heavy-tailed Lévy distribution (Viswanathan et al., 1999). In a similar manner, fracture center locations in the Lévy-Lee algorithm are produced by random walk, and the distance between fracture centers L' is sampled from the power law distribution:

$$P_L(L' > L) = L^{-D} \quad (7)$$

where D is a specified fractal dimension. The direction of the separation between fracture centers is uniformly distributed between 0° and 360° . Fracture length and the variation in orientation are proportional to the distance from the previous fracture. The Lévy-Lee model generates a fracture network with a continuum of scales for both fracture length and spacing between fractures and uses the same exponent for fracture trace length and spacing. Structurally, the fracture networks generated by the Lévy-Lee algorithm tend to have clusters of fractures, with tighter clusters resulting from larger values of D .

This mesh was then mapped onto a 3-D grid and extended across the width of the domain in the y direction – a single cell across – since FEHM does not solve true 2-D problems. This mapping essentially embeds the fractures in the rock matrix via upscaling of properties, allowing transfer of fluids and tracers to occur at the fracture-matrix interface. This mesh was then mapped onto a uniform grid. This mapping essentially embeds the fractures in the rock matrix via upscaling of properties, allowing transfer of gas tracers to occur at the fracture-matrix interface. The upscaling procedure is described below in Section 4.2.

4.2. Upscaling of Properties

Background rock matrix in the base case was assigned a porosity (ϕ_m) of 35%, which is in the range previously estimated based on consideration of the low bedrock density at Gale crater (Lewis et al., 2019). We set the background rock permeability (k_m) to $1 \times 10^{-14} \text{ m}^2$ (0.01 Darcies). This is slightly more permeable than the conservative $3 \times 10^{-15} \text{ m}^2$ prescribed by previous research modeling hydrothermal circulation on Mars (Lyons et al., 2005), which is appropriate as our domain is much shallower than the domain considered there (~ 10 km), and permeability tends to decrease with depth (Manning & Ingebritsen, 1999). Fracture porosity (ϕ_f) was assumed 100% for open fractures; fracture permeability

(k_f) was derived via the “cubic law” ($k_f = b^2/12 = 8.3 \times 10^{-10} \text{ m}^2$) given a prescribed fracture aperture (b) of 0.1 mm for all fractures in the domain. Rover photographs of bedrock fractures often show fracture apertures in the range of 1-2 cm (Figures S6, S5). However, these photographs are nearly always of fractures expressed at the planet’s surface, where they are potentially exposed to freeze-thaw cycles and dehydration of the surrounding rocks, which will cause the fracture apertures to expand. These processes are not as active below the surface, so fracture apertures at depth will be comparatively narrower. Furthermore, at least in the shallow subsurface, fractures tend to be somewhat infilled by dust and/or unconsolidated material S5 such that the effective permeability of the fracture is less than that predicted by the cubic law. These factors combined with the fact that lithostatic pressure, a force that tends to close fractures, increases with depth, lead us to prescribe uniform 0.1 mm fracture apertures as a conservative estimate for Mars’ subsurface. Fracture permeability k_f is upscaled using:

$$k_f = \frac{b^3}{12\Delta x} \quad (8)$$

where b is the assumed fracture aperture (m) and Δx is the grid/cell block size (m). Upscaled to the grid dimensions of the numerical mesh, the modeled (effective) fracture permeability was $8.3 \times 10^{-14} \text{ m}^2$. We upscale fracture porosity using a flow-weighted scheme (Birdsell et al., 2015):

$$\phi_f = \frac{b}{\Delta x} \quad (9)$$

giving a model (effective) fracture porosity of 0.0001 (0.01%) at the scale of the computational grid. The upscaled relationships (8) and (9) consistently allow the simulation of the governing equations (1) - (6) for fractures and matrix using a porous media simulator such as FEHM. This approach is widely used for simulation of flow and transport in fractured rock (Chaudhuri et al., 2013; Fu et al., 2016; Pandey & Rajaram, 2016; Haagensohn & Rajaram, 2021).

4.3. Fracture Network Topology

The fracture network used in this study was designed to be representative of a fractured subsurface on Mars. Without rock cores or detailed logs, we know very little about fracture networks on Mars below the surface, though it is believed to be highly fractured (Figure S5). We want to generate a fracture network such that it would have a fracture density (i.e., the ratio of fracture volume to bulk rock volume) comparable to that in Mars’ subsurface. Because the subsurface on Mars is so poorly characterized, we have made estimates of the fracture density based on rover photographs depicting surface expressions of fracture networks at Gale crater using a fracture trace method (Figure S6). Because the observed surface is roughly two-dimensional – and also due to the 2-D nature of our model – we calculate an “areal fracture density” (the ratio of fracture area to bulk rock area) and assume a similar fracture distribution in cross-section. The areal fracture density of the fracture network used herein was $\sim 0.1\%$. We track the area of the fracture traces relative to the total image area using a script in Adobe Illustrator (Adobe Inc., 2019).

We also ran one simulation with depth-dependent fracture density to test the effect of reduced fracture density with depth. We generally expect lower fracture density at depth because lithostatic pressure increases with depth, and will thus tend to close fractures. We generated a depth-dependent fracture density mesh somewhat simplistically, using the base case fracture network topology as a starting point. We broke up the domain vertically into thirds and randomly removed 55% of fractures from the middle third, and 95% of fractures from the bottom third, leaving the top third of the model (i.e., the shallowest portion) untouched (Figure S7).

5. Correlation Between Atmospheric Abundance and Surface Flux

Our subsurface transport model simulates surface fluxes rather than atmospheric concentrations. Thus, we cannot directly evaluate the model against observed atmospheric methane abundances. However, atmospheric concentrations are supplied by surface fluxes, and it is thus reasonable to expect some correlation between integrated surface fluxes and atmospheric abundance. The influence of wind, atmospheric mixing rates, planetary boundary layer (PBL) height, photochemical destruction, and other factors could complicate the analysis of such correlations. Nevertheless, we did find a linear between simulated surface flux and the atmospheric methane abundance measurements from *Curiosity* (Webster et al., 2018), the analysis for which is presented below.

Atmospheric methane abundance measurements from *Curiosity* are taken from Webster et al. (2018). For the simulated surface fluxes, we performed a window rolling mean (moving average) in order to get the approximate integral of mass flux at the time of the atmospheric measurements. We analyzed correlations using a range of window sizes (from 50-2000 samples) for the rolling mean approximation of surface methane flux, all to similar effect.

5.1. Cross-correlation

Calculating the cross-correlation of atmospheric abundance measurements to simulated surface flux theoretically provides insight into the time lag between changes in flux and the corresponding change in atmospheric concentration (if one exists). Because of vertical mixing times in the atmospheric column after subsurface release, we would intuitively suppose some amount of lag between changes in the surface flux integral and the resultant atmospheric methane concentration. Due to factors such as photochemical destruction and lateral transport away from the seepage area, we would also assume that after sufficient lag time, changes in surface flux would have very little correlation with changes in atmospheric concentration. However, with only 10 abundance measurements, determining the true lag is not possible. Nevertheless, we performed a cross-correlation analysis in the hopes of estimating any lag in correlation between abundance and flux.

For this analysis, we interpolated the methane abundance measurements to uniform spacing in L_s . We then interpolated the surface flux rolling mean to the same L_s and performed the cross-correlation analysis. The results presented here used a window size for simulated flux of 500 samples, which for our data encapsulates a solar longitude (L_s) window of about 0.5° , or approximately 1 sol. The results of the cross-correlation are presented in Figure S8c. Maximum correlation occurs at lag 0 (0°), with a secondary maximum occurring at lag 1 ($\sim 36^\circ$, or about 66 sols), with abundance lagging surface flux in this case. Because of insufficient temporal resolution in the abundance measurements, it is not possible to better estimate the lag in the atmospheric concentration. We can, however, say with some degree of confidence that the lag in correlation is likely between $0-36^\circ L_s$ ($\sim 0-66$ sols).

Previous research by Moores et al. (2019) calibrated an adsorption-diffusion model by coupling surface flux to an atmospheric column and comparing the results to the atmospheric abundance measurements from Webster et al. (2018). To balance the accumulation of methane in the atmosphere, they included a lumped term called the effective atmospheric dissipation timescale (EADT) that approximates the lifetime of near-surface atmospheric methane in the model, and implicitly combines the effects of mixing, advection, and photolysis by destructive processes. They found best fits to the background methane abundance measurements when they prescribed EADT values between an order of ~ 10 and ~ 100 sols. Mass balance dictates that greater methane seepage requires a shorter methane atmospheric lifetime (i.e., smaller EADT). Although our model doesn't calculate atmospheric concentrations resulting from subsurface-to-atmospheric seepage, it makes sense that the lag in our cross-correlation would fall on the smaller end of that range since our base case fluxes were similar to the upper limit estimated by Moores et al. (2019), which in their work corresponded to an EADT on the order of tens of sols. A direct comparison between EADT and cross-correlation lag can not be made here, but the lag in correlation between flux and atmospheric abundance could likely be related to some measure of methane lifetime in the atmospheric column.

5.2. Linear Correlation

The cross-correlation analysis above showed maximum correlation of atmospheric abundance and surface flux between a temporal lag of $0-36^\circ L_s$ ($\sim 0-66$ sols). Though the temporal resolution in atmospheric abundance measurements was limited, this result highlights that a linear correlation analysis could be illustrative.

We present the linear correlation, again using a window size of 500 samples (Figure S9). We calculated a Pearson correlation coefficient of 0.62, which indicates a reasonable degree of linear correlation between surface flux and atmospheric concentration. Greater surface fluxes generally correspond to elevated atmospheric concentrations, which makes intuitive sense from a mass balance perspective (assuming the atmospheric gases are supplied by the subsurface); higher surface fluxes integrated with respect to time result in an increase in methane supplied to the atmosphere.

The low coefficient of determination ($R^2 = 0.39$) indicates that a linear model does not very well predict atmospheric abundance given only the surface flux. Deviations from a pure linear relationship could be due to a number of factors: time-varying atmospheric mixing times, methane destruction mechanisms,

local disturbances such as wind, other potential nearby sources of methane, as well as the fact that the rover was changing location in between measurements. These co-dependencies make it difficult to predict atmospheric concentrations from instantaneous surface flux calculations alone.

6. Additional Results

To conserve space in the main text, we here include surface flux time-series plots for the simulations other than the base case (described in main article). We also include the results of two simulations analogous to the base case, but having shallower methane source depths (150 m, 50 m), a simulation having narrower fractures (aperture $b = 0.01$ mm), a simulation having wider fractures ($b = 1$ mm), a case with much higher methane production rates (6.7×10^{-12} mol CH₄ m⁻³ s⁻¹) in the source zone, as well as a case having depth-dependent fracture density (see Figure S7). It should be noted that the sensitivity of subsurface transport to geologic properties is highly non-linear. The transport efficiency of the subsurface is sensitive to the interaction between geologic parameters (source depth, ϕ_m , k_m , b , and fracture density, among others) as well as the amplitude and frequency of the atmospheric forcing. We have simulated a number of different scenarios for illustration, but they do not fully describe the sensitivity of transport in this system to changes in geologic properties.

The high- k_m case (Figure S10) had time-averaged fluxes greater than those of the base case. Time-averaged flux over the 334-sol window was $\sim 120\%$ greater. This follows generally from the discussion in (Nilson et al., 1991) regarding bulk diffusivity of the subsurface as a function of matrix permeability: the bulk diffusivity reaches a plateau beyond a certain matrix permeability, so despite the 2-order-of-magnitude permeability increase, we would not expect outside changes in the ability of the subsurface to breathe with increasing matrix permeability.

The low- k_m case (Figure S11) had between 36-53% lower time-averaged flux than the base case depending on window size. In general, we would expect lower matrix permeability to result in an increase in bulk diffusivity since the pressure waves will propagate more efficiently in the fracture network if they are damped to a lesser extent by fracture-matrix interaction, which extracts air from fractures to the rock matrix (Nilson et al., 1991). It is possible that because of the relatively high matrix porosity ($\phi_m = 35\%$), the large capacitance volume in the rock matrix is unable to provide a sufficiently large portion of methane to the fractures because of the lower matrix permeability, which limits the penetration distance of the invading air.

The low- ϕ_m case (Figure S12) had time-averaged flux roughly 30x smaller compared to the base case. This is somewhat counter-intuitive, as we would expect a higher matrix porosity (ϕ_m) to mean that air propagating through fractures has more matrix pore volume to equilibrate with in order to extract tracer mass. With a lower matrix porosity, we expect a greater diffusive exchange efficiency, whereby a greater portion of the subsurface tracer is extracted each cycle. In this instance, it seems that the matrix is participating a great deal in gas transport, such that the increased storage capacity of the rock adjacent to the fractures enhances transport on the whole. The ratcheting mechanism is facilitated by having greater matrix storage.

In the 50-m shallow source case (Figure S13) we considered, time-averaged fluxes were approximately 190% greater than those in the base case. This is not surprising, as we would expect a shallower source to produce greater surface fluxes. Note that if we were to consider an unsteady system (e.g., one in which the methane source produced gas infrequently), there would be a larger difference between shallow and base cases – in favor of the shallow source – since the time of first arrival of methane at the surface would occur correspondingly faster. For the 150-m shallow source case (Figure S14), time-averaged fluxes were approximately 1% greater than those in the base case.

For the narrow fracture case (Figure S15), time-averaged fluxes in northern summer were approximately one order of magnitude lower than in the base case. Fracture transmissivity is highly sensitive to the fracture aperture, with a cubic dependence (2), so this result is not surprising. It is of some interest that the time-averaged fluxes in northern winter are slightly more than 2 orders of magnitude lower than in the base case. The smaller fracture aperture creates a much smaller bulk diffusivity, which limits methane outflux to the times of greatest pressure fluctuation. For the same reason, it is not surprising that the wider fracture aperture case (Figure S16) yielded much greater fluxes.

The high methane-production rate simulation (Figure S17) unsurprisingly resulted in much greater surface methane fluxes (approximately 500x greater) than in the base case. The production rate in the source zone for this scenario is much greater than can likely be produced by extant methanogens or serpentinization reactions on Mars. However, this simulation highlights the importance of the source

strength in regulating subsurface fluxes, while also pointing to the fact that barometric pumping could promote very high surface fluxes of gases released from high-intensity sources.

The depth-dependent fracture density simulation (Figure S18) resulted in surface methane fluxes comparable to the base case, though still approximately 10% greater. For the subsurface parameters we used, it seems that having a less-diffuse fracture network at depth allowed for more efficient transport to the shallow regions of the model. This makes some intuitive sense; fewer high-permeability pathways at depth should bring methane up to the mid- and shallow-depths in greater concentration than if there were many branching fractures, which tend to disperse tracers. At shallower depths, where the transportation potential by barometric fluctuations is strongest, the comparatively higher fracture density should allow large quantities of methane to then be transmitted to the atmosphere.

References

- Adobe Inc. (2019). *Adobe Illustrator* [Software]. Retrieved from <https://adobe.com/products/illustrator>
- Birdsell, D. T., Rajaram, H., Dempsey, D., & Viswanathan, H. S. (2015). Hydraulic fracturing fluid migration in the subsurface: A review and expanded modeling results. *Water Resources Research*, *51*(9), 7159–7188. doi: 10.1002/2015WR017810
- Boston, P. J., Ivanov, M. V., & McKay, C. P. (1992). On the Possibility of Chemosynthetic Ecosystems in Subsurface Habitats on Mars. *Icarus*, *95*(2), 300–308.
- Carrier, B. L., Beaty, D. W., Meyer, M. A., Blank, J. G., Chou, L., Dassarma, S., ... Xu, J. (2020). Mars Extant Life: What's Next? Conference Report. *Astrobiology*, *20*(6), 785–814. doi: 10.1089/ast.2020.2237
- Chaudhuri, A., Rajaram, H., & Viswanathan, H. (2013). Early-stage hypogene karstification in a mountain hydrologic system: A coupled thermohydrochemical model incorporating buoyant convection. *Water Resources Research*, *49*(9), 5880–5899. doi: 10.1002/wrcr.20427
- Clemo, T. M., & Smith, L. (1997). A hierarchical model for solute transport in fractured media. *Water Resources Research*, *33*(8), 1763–1783.
- Cooley, J. W., & Tukey, J. W. (1965). An Algorithm for the Machine Calculation of Complex Fourier Series. *Mathematics of Computation*, *19*(90), 297–301. doi: 10.2307/2003354
- Fu, P., Hao, Y., Walsh, S. D., & Carrigan, C. R. (2016). Thermal Drawdown-Induced Flow Channeling in Fractured Geothermal Reservoirs. *Rock Mechanics and Rock Engineering*, *49*(3), 1001–1024. doi: 10.1007/s00603-015-0776-0
- Fung, L.-K., Hiebert, A. D., & Nghiem, L. X. (1992). Reservoir simulation with a control-volume finite-element method. *SPE Reservoir Engineering*, *7*(03), 349–357.
- Geier, J. E., Lee, K., & Dershowitz, W. S. (1988). Field validation of conceptual models for fracture geometry. *Transactions of American Geophysical Union*, *69*(44), 1177.
- Haagenson, R., & Rajaram, H. (2021). Seismic Diffusivity and the Influence of Heterogeneity on Injection-Induced Seismicity. *Journal of Geophysical Research: Solid Earth*, *126*(6). doi: 10.1029/2021JB021768
- Jones, E. G., Lineweaver, C. H., & Clarke, J. D. (2011). An extensive phase space for the potential Martian biosphere. *Astrobiology*, *11*(10), 1017–1033. doi: 10.1089/ast.2011.0660
- Kronyak, R. E., Kah, L. C., Edgett, K. S., VanBommel, S. J., Thompson, L. M., Wiens, R. C., ... Nachon, M. (2019). Mineral-Filled Fractures as Indicators of Multigenerational Fluid Flow in the Pahrump Hills Member of the Murray Formation, Gale Crater, Mars. *Earth and Space Science*, *6*(2), 238–265. doi: 10.1029/2018EA000482
- Lewis, K. W., Peters, S., Gonter, K., Morrison, S., Schmerr, N., Vasavada, A. R., & Gabriel, T. (2019). A surface gravity traverse on Mars indicates low bedrock density at Gale crater. *Science*, *363*(6426), 535–537. doi: 10.1126/science.aat0738
- Lin, L. H., Hall, J., Onstott, T. C., Gihring, T., Lollar, B. S., Boice, E., ... Bellamy, R. E. (2006). Planktonic microbial communities associated with fracture-derived groundwater in a deep gold mine of South Africa. *Geomicrobiology Journal*, *23*(6), 475–497. doi: 10.1080/01490450600875829
- Lollar, B. S., Lacrampe-Couloume, G., Slater, G. F., Ward, J., Moser, D. P., Gihring, T. M., ... Onstott, T. C. (2006). Unravelling abiogenic and biogenic sources of methane in the Earth's deep subsurface. *Chemical Geology*, *226*(3-4), 328–339. doi: 10.1016/j.chemgeo.2005.09.027
- Lyons, J. R., Manning, C. E., & Nimmo, F. (2005). Formation of methane on Mars by fluid-rock interaction in the crust. *Geophysical Research Letters*, *32*(13), 1–4. doi: 10.1029/2004GL022161

- Manning, C. E., & Ingebritsen, S. E. (1999). Permeability of the Continental Crust: Implications of Geothermal Data and Metamorphic Systems. *Reviews of Geophysics*, *37*(1), 127–150.
- Mellon, M. T., & Phillips, R. J. (2001). Recent gullies on Mars and the source of liquid water. *Journal of Geophysical Research E: Planets*, *106*(E10), 23165–23179. doi: 10.1029/2000JE001424
- Moore, J. E., Gough, R. V., Martinez, G. M., Meslin, P. Y., Smith, C. L., Atreya, S. K., . . . Webster, C. R. (2019). Methane seasonal cycle at Gale Crater on Mars consistent with regolith adsorption and diffusion. *Nature Geoscience*, *12*(5), 321–325. doi: 10.1038/s41561-019-0313-y
- Nilson, R. H., Peterson, E. W., Lie, K. H., Burkhard, N. R., & Hearst, J. R. (1991). Atmospheric Pumping: A Mechanism Causing Vertical Transport of Contaminated Gases Through Fractured Permeable Media. *Journal of Geophysical Research: Solid Earth*, *96*(B13), 933–948. doi: 10.2752/147597509112541
- Oehler, D. Z., & Etiop, G. (2017). Methane seepage on Mars: where to look and why. *Astrobiology*, *17*(12), 1233–1264. doi: 10.1089/ast.2017.1657
- Pandey, S., & Rajaram, H. (2016). Modeling the influence of preferential flow on the spatial variability and time-dependence of mineral weathering rates. *Water Resources Research*, *52*(12), 9344–9366. doi: 10.1111/j.1752-1688.1969.tb04897.x
- Stamenković, V., Beegle, L. W., Zacny, K., Arumugam, D. D., Baglioni, P., Barba, N., . . . Woolley, R. (2019). The next frontier for planetary and human exploration. *Nature Astronomy*, *3*(2), 116–120. Retrieved from <http://dx.doi.org/10.1038/s41550-018-0676-9> doi: 10.1038/s41550-018-0676-9
- Stamenković, V., Ward, L. M., Mischna, M. A., & Fischer, W. W. (2019). Mars Extant Life: What’s Next? *LPI Contributions*, *2108*, 41550.
- Tung, H. C., Bramall, N. E., & Price, P. B. (2005). Microbial origin of excess methane in glacial ice and implications for life on Mars. *Proceedings of the National Academy of Sciences of the United States of America*, *102*(51), 18292–18296. doi: 10.1073/pnas.0507601102
- Viswanathan, G. M., Buldyrev, S. V., Havlin, S., Da Luz, M. G., Raposo, E. P., & Stanley, H. E. (1999). Optimizing the success of random searches. *Nature*, *401*(6756), 911–914. doi: 10.1038/44831
- Webster, C. R., Mahaffy, P. R., Atreya, S. K., Moore, J. E., Flesch, G. J., Malespin, C., . . . Navarro-Gonzalez, R. (2018). Background levels of methane in Mars’ atmosphere show strong seasonal variations. *Science*, *360*(6393), 1093–1096.
- Zimmerman, R. W., & Bodvarsson, G. S. (1996). Hydraulic Conductivity of Rock Fractures. *Transport in Porous Media*, *23*(1), 1–30.
- Zyvoloski, G. A. (2007). *FEHM: A control volume finite element code for simulating subsurface multi-phase multi-fluid heat and mass transfer* (Tech. Rep.). Los Alamos, NM: Los Alamos National Laboratory.
- Zyvoloski, G. A., Robinson, B. A., Dash, Z. V., Kelkar, S., Viswanathan, H. S., Pawar, R. J., . . . Chu, S. (2021). *Software users manual (UM) for the FEHM application version 3.1-3X*. Los Alamos, NM: Los Alamos National Laboratory Report LA-UR-12-24493.

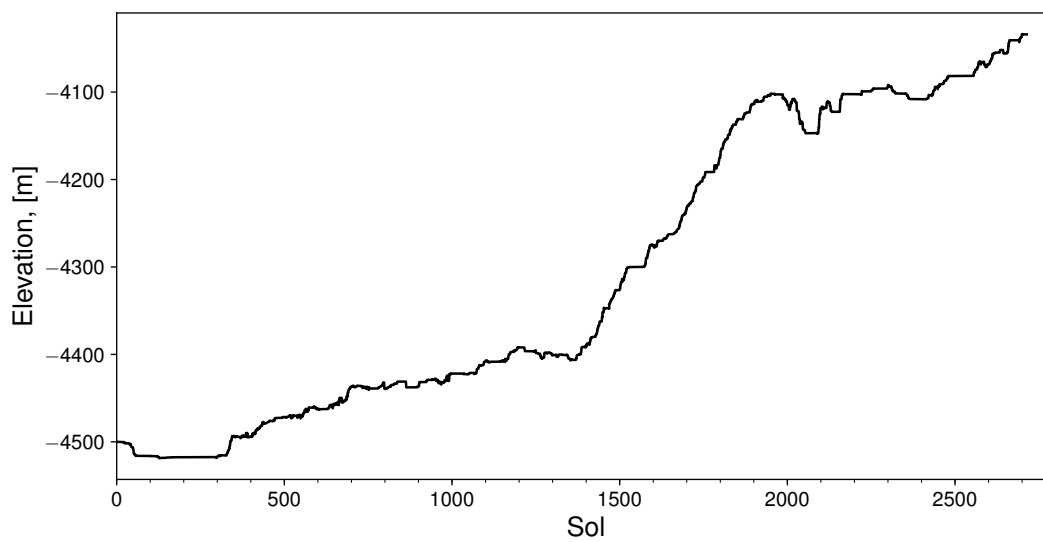


Figure S1. *Curiosity* rover elevation data in time used for elevation-pressure correction. Negative elevation is in reference to the Mars datum (Mars average elevation).

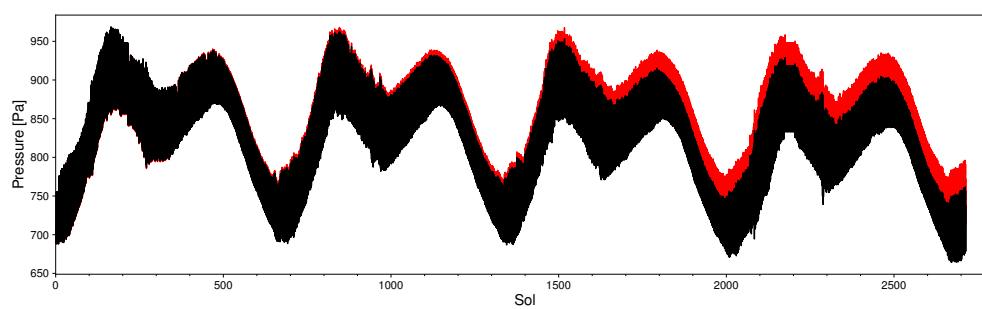


Figure S2. Raw pressure data (**black**) and elevation-corrected data (**red**).

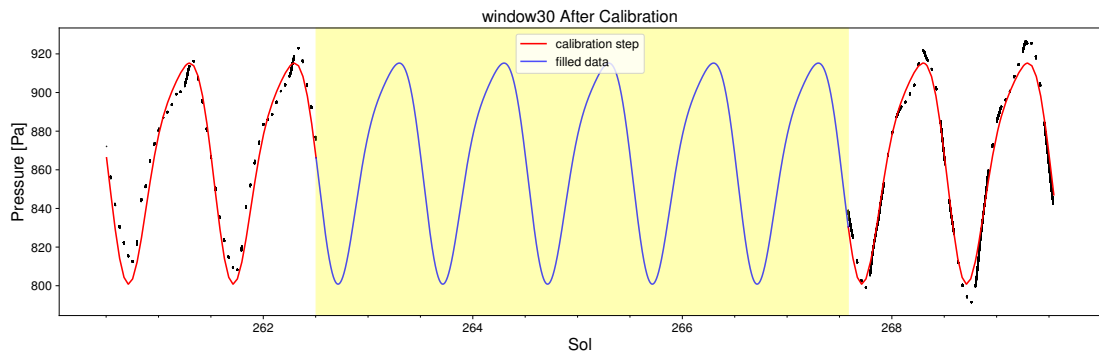


Figure S3. An example window selected in the barometric data gap-filling procedure. Highlighted area represents the span of the data gap being filled, red line is the Fourier series calibrated to non-missing data, and the blue line is the synthetic Fourier series used to fill the data gap.

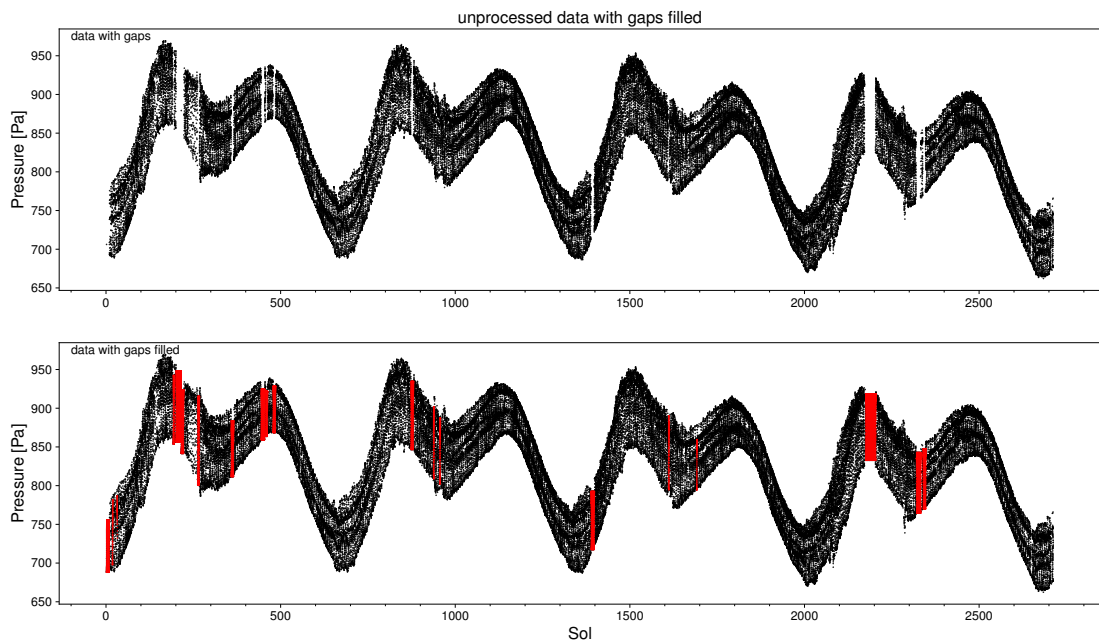


Figure S4. Results of the barometric data gap-filling procedure: (top) unprocessed data; (bottom) gaps filled with synthetic Fourier series data in red.

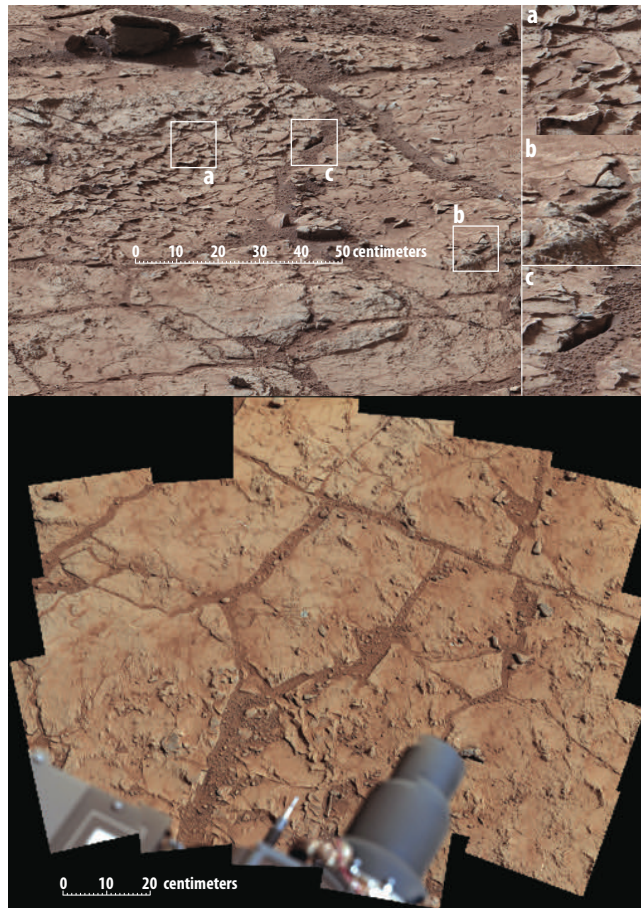


Figure S5. Examples of macroscopic surface fractures at Gale crater photographed by *Curiosity*'s Mastcam. (Top) A view of a patch of veined, flat-lying rock selected as the first drilling site for *Curiosity*, taken on sol 153 in the Yellowknife Bay geologic formation. Three boxes, each about 10 cm across, designate enlargements illustrating attributes of the area: (a) a high concentration of ridge-like veins protruding above the surface, with some veins having two walls and an eroded interior; (b) a horizontal discontinuity a few centimeters beneath the surface, which may be a bed, a fracture, or a horizontal vein; (c) a hole developed in the sand overlying a fracture, which implies a shallow infiltration of sand down into the fracture system. (Bottom) mosaic of the area, called "John Klein", where the rover performed its first sample drilling. Surface expression of these fractures show apertures on the scale of 1-2 cm, with most of the fracture volume occupied by unconsolidated material filling. Image credits: (top) NASA/JPL-Caltech/MSSS; (bottom) NASA/JPL-Caltech/MSSS.

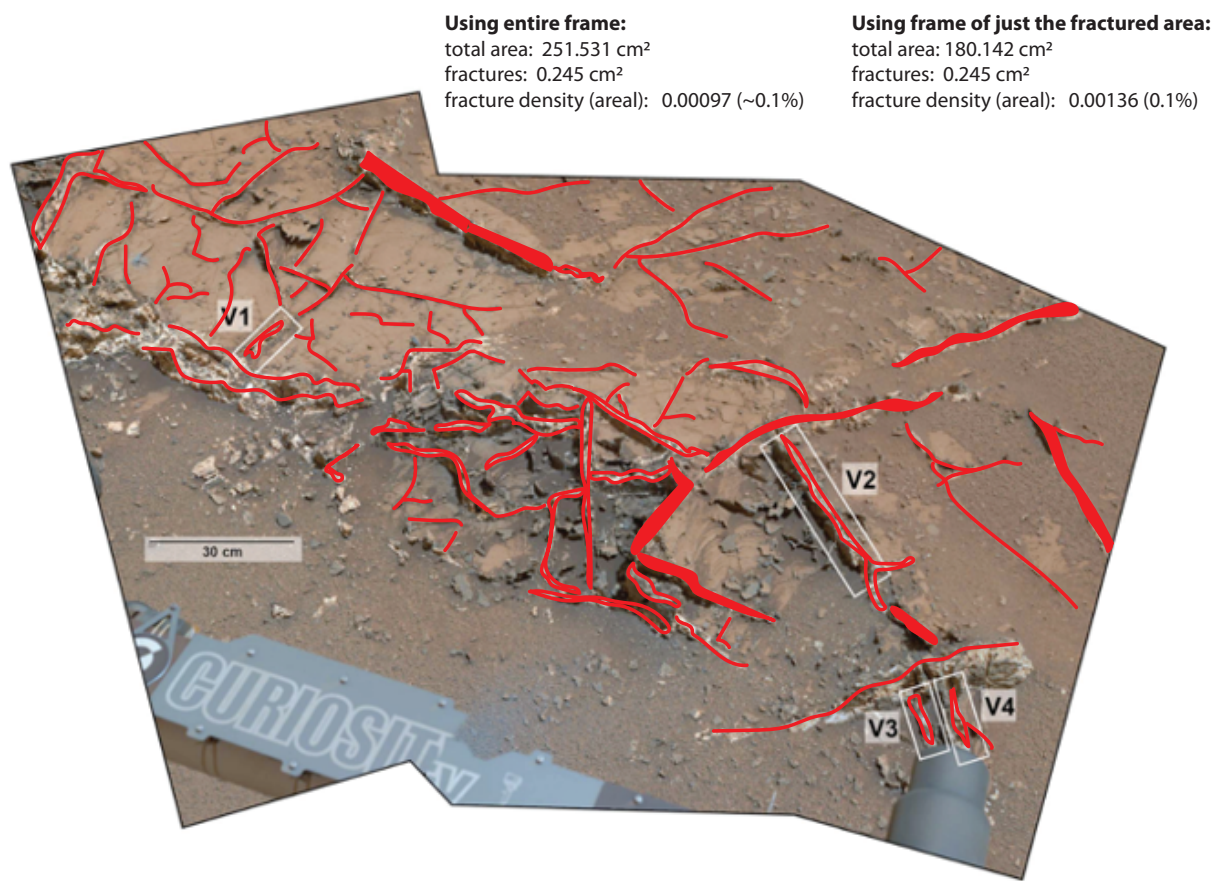


Figure S6. Fracture trace method used to approximate the areal “fracture density” of Mars’ subsurface, applied to a Mastcam-34 mosaic (Kronyak et al., 2019) of the Garden City vein (mineral-filled fracture) complex at Gale crater. Centimeter-thick sandwich veins comprise the positive-relief intersecting network. Note that annotated areal dimensions are based on screen dimensions rather than the physical outcrop.

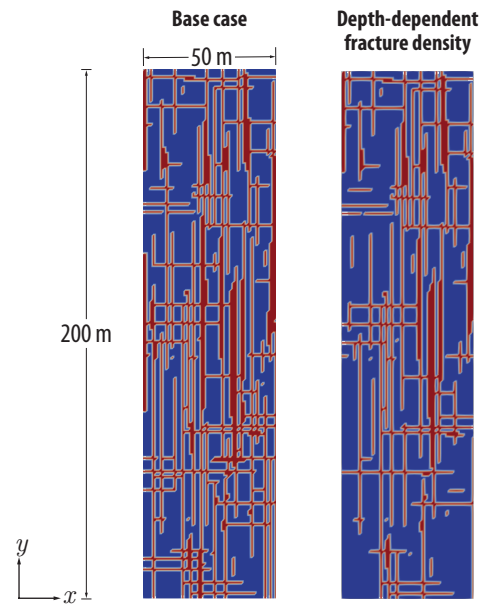


Figure S7. Comparison of fracture network topology for the base case (left) and the depth-dependent fracture density case (right).

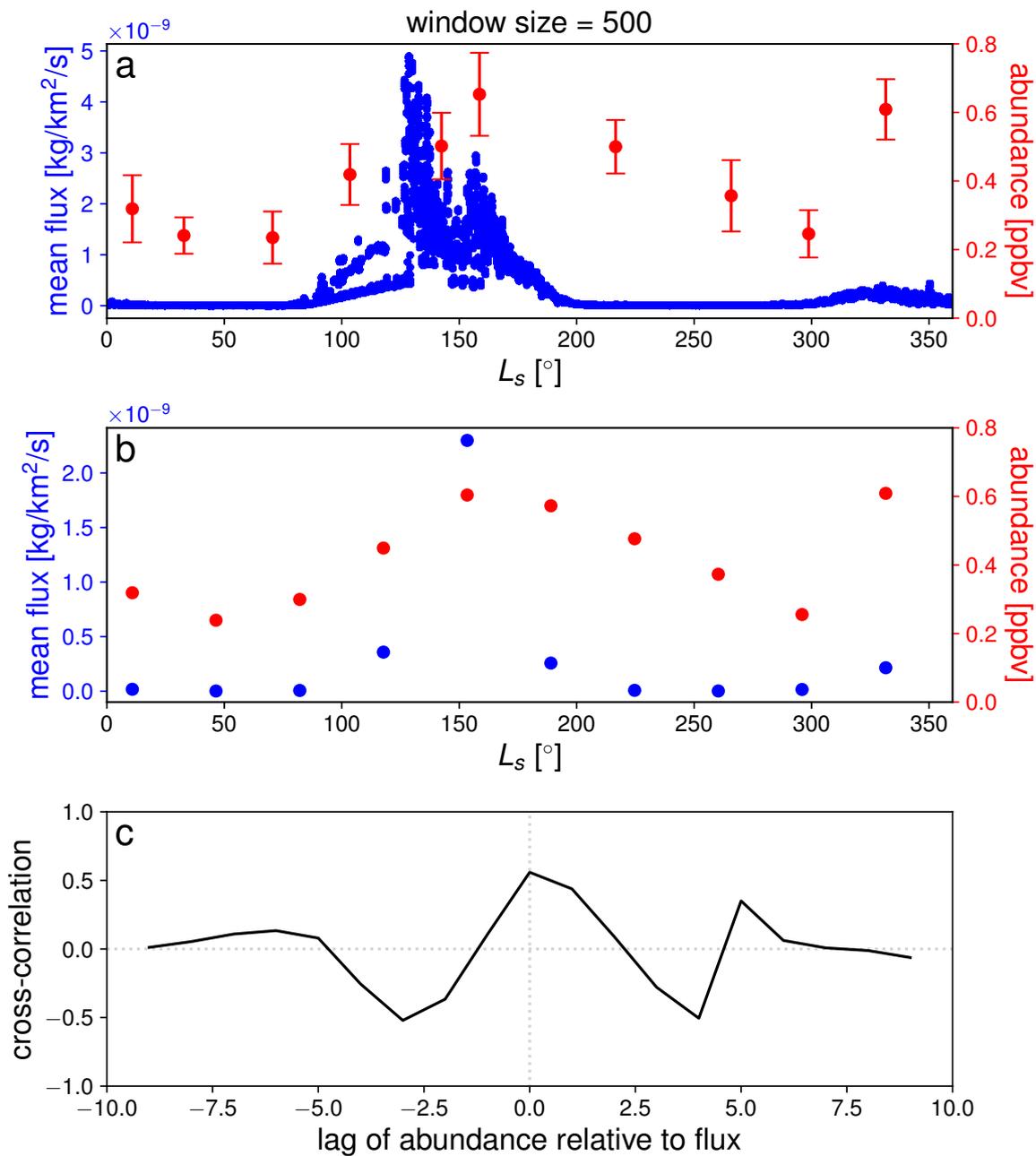


Figure S8. (a) Rolling mean surface flux (blue) and the actual atmospheric abundance measurements (red); (b) rolling mean surface flux (blue) and the atmospheric abundance (red) interpolated to uniform spacing in solar longitude (L_s); (c) cross-correlation of atmospheric abundance with surface flux.

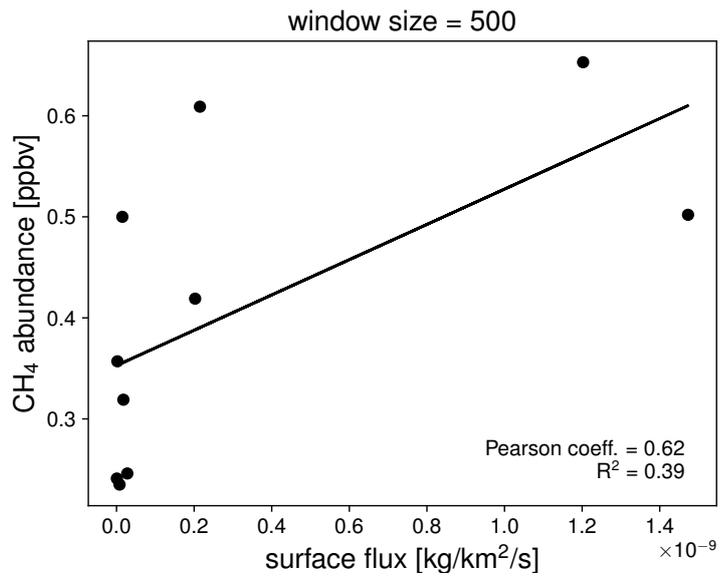


Figure S9. Solid line shows best-fit linear correlation between atmospheric methane abundance measurements and simulated surface flux.

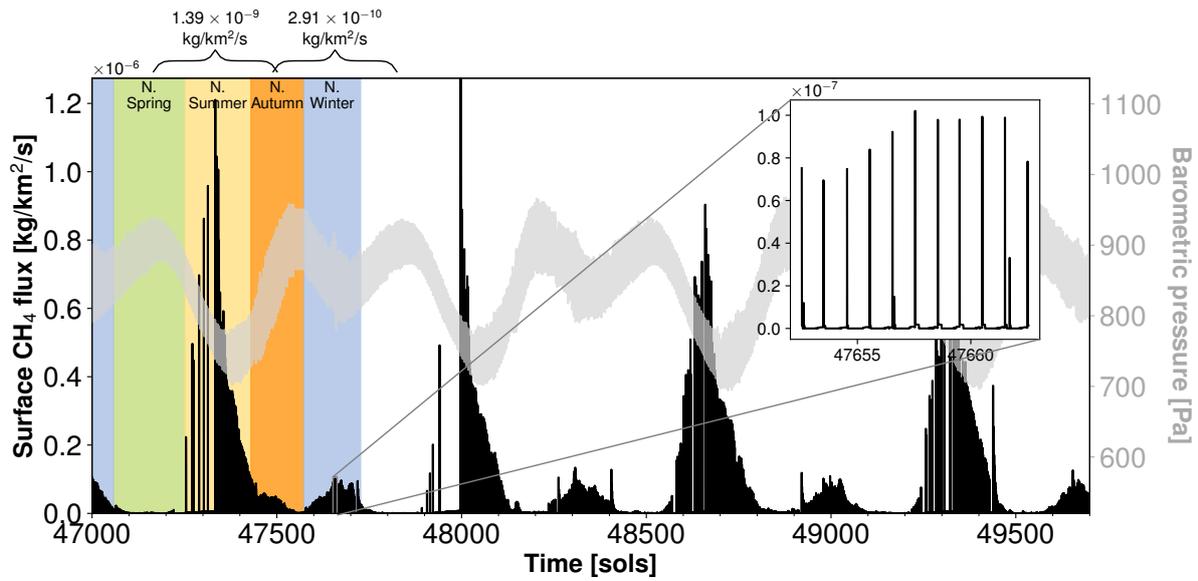


Figure S10. High- k_m case methane flux (**black**), with barometric pressure forcing (**gray**) driving the subsurface transport model. Annotations in-figure with curly braces indicate time-averaged fluxes for the 334-sol spans shown, each centered on the local flux maximum. Colored zones indicate Mars seasons for the northern hemisphere. Inset figure highlights the diurnal and semi-diurnal variations in surface methane flux.

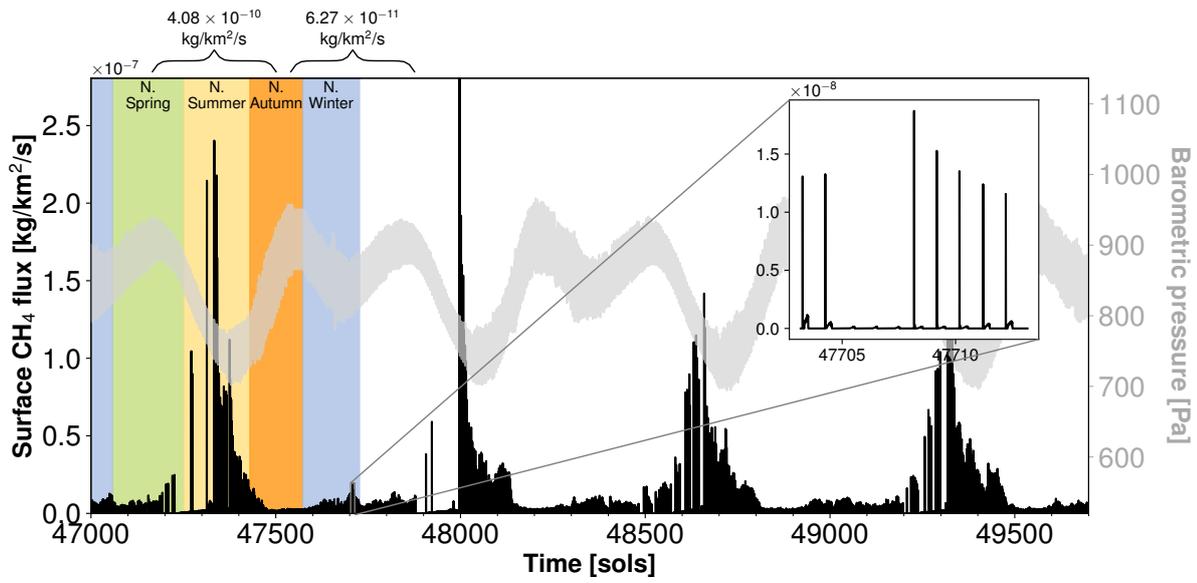


Figure S11. Low- k_m case methane flux (**black**), with barometric pressure forcing (**gray**) driving the subsurface transport model. Annotations in-figure with curly braces indicate time-averaged fluxes for the 334-sol spans shown, each centered on the local flux maximum. Colored zones indicate Mars seasons for the northern hemisphere. Inset figure highlights the diurnal and semi-diurnal variations in surface methane flux.

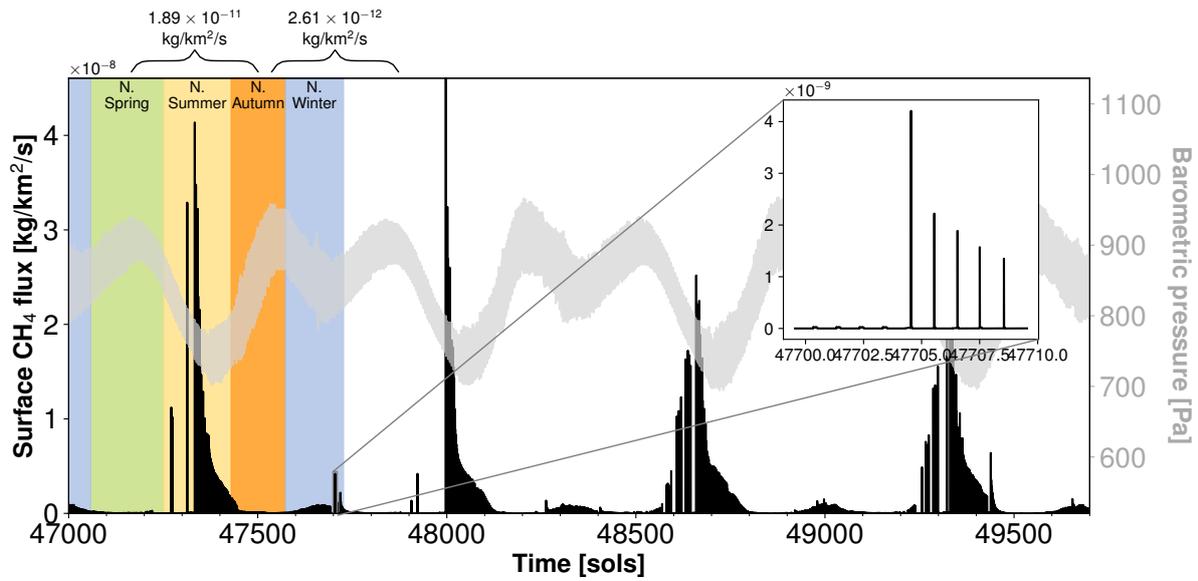


Figure S12. Low- ϕ_m case methane flux (**black**), with barometric pressure forcing (gray) driving the subsurface transport model. Annotations in-figure with curly braces indicate time-averaged fluxes for the 334-sol spans shown, each centered on the local flux maximum. Colored zones indicate Mars seasons for the northern hemisphere. Inset figure highlights the diurnal and semi-diurnal variations in surface methane flux.

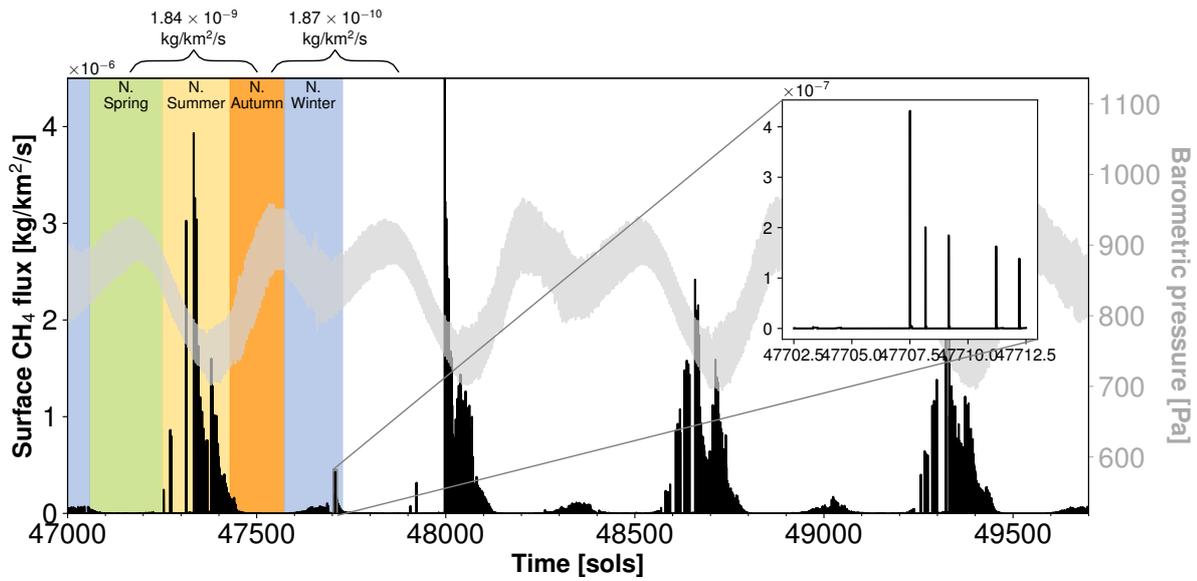


Figure S13. Shallow-source (50 m) case methane flux (**black**), with barometric pressure forcing (gray) driving the subsurface transport model. Hydrogeologic properties are otherwise identical to the base case simulation. Annotations in-figure with curly braces indicate time-averaged fluxes for the 334-sol spans shown, each centered on the local flux maximum. Colored zones indicate Mars seasons for the northern hemisphere. Inset figure highlights the diurnal and semi-diurnal variations in surface methane flux.

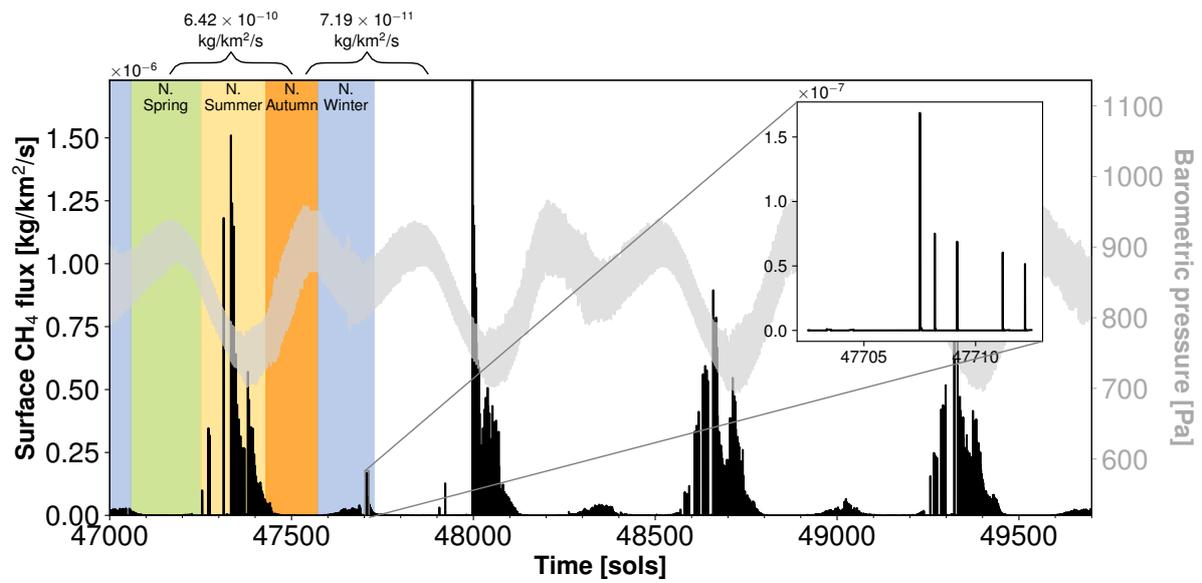


Figure S14. Shallow-source (150 m) case methane flux (**black**), with barometric pressure forcing (**gray**) driving the subsurface transport model. Hydrogeologic properties are otherwise identical to the base case simulation. Annotations in-figure with curly braces indicate time-averaged fluxes for the 334-sol spans shown, each centered on the local flux maximum. Colored zones indicate Mars seasons for the northern hemisphere. Inset figure highlights the diurnal and semi-diurnal variations in surface methane flux.

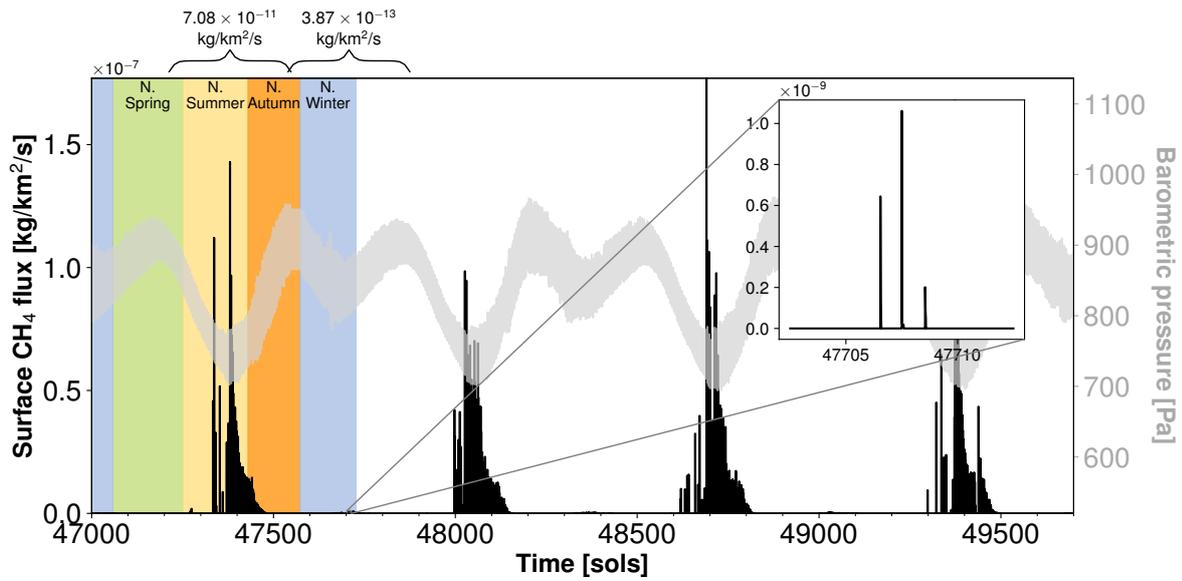


Figure S15. Narrow-fractures (aperture $b = 0.01$ mm) case methane flux (**black**), with barometric pressure forcing (gray) driving the subsurface transport model. Following from cubic law (2), this fracture aperture yields a fracture permeability (k_f) of 8.3×10^{-12} m². Hydrogeologic properties are otherwise identical to the base case simulation. Annotations in-figure with curly braces indicate time-averaged fluxes for the 334-sol spans shown, each centered on the local flux maximum. Colored zones indicate Mars seasons for the northern hemisphere. Inset figure highlights the diurnal and semi-diurnal variations in surface methane flux.

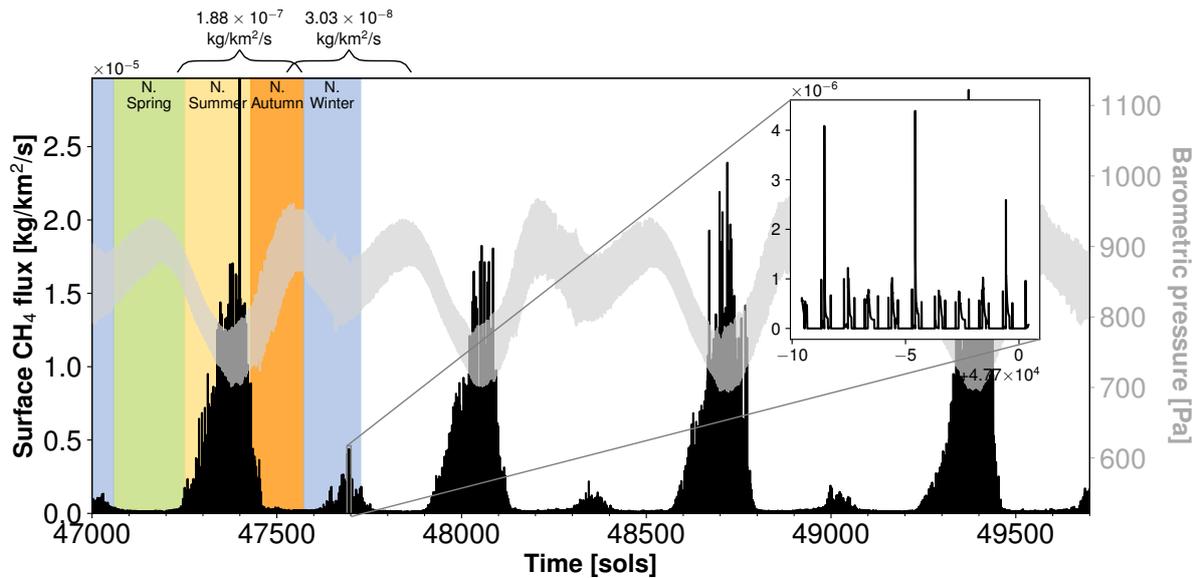


Figure S16. Wide-fractures (aperture $b = 1.0$ mm) case methane flux (**black**), with barometric pressure forcing (gray) driving the subsurface transport model. Following from cubic law (2), this fracture aperture yields a fracture permeability (k_f) of 8.3×10^{-8} m². Hydrogeologic properties are otherwise identical to the base case simulation. Annotations in-figure with curly braces indicate time-averaged fluxes for the 334-sol spans shown, each centered on the local flux maximum. Colored zones indicate Mars seasons for the northern hemisphere. Inset figure highlights the diurnal and semi-diurnal variations in surface methane flux.

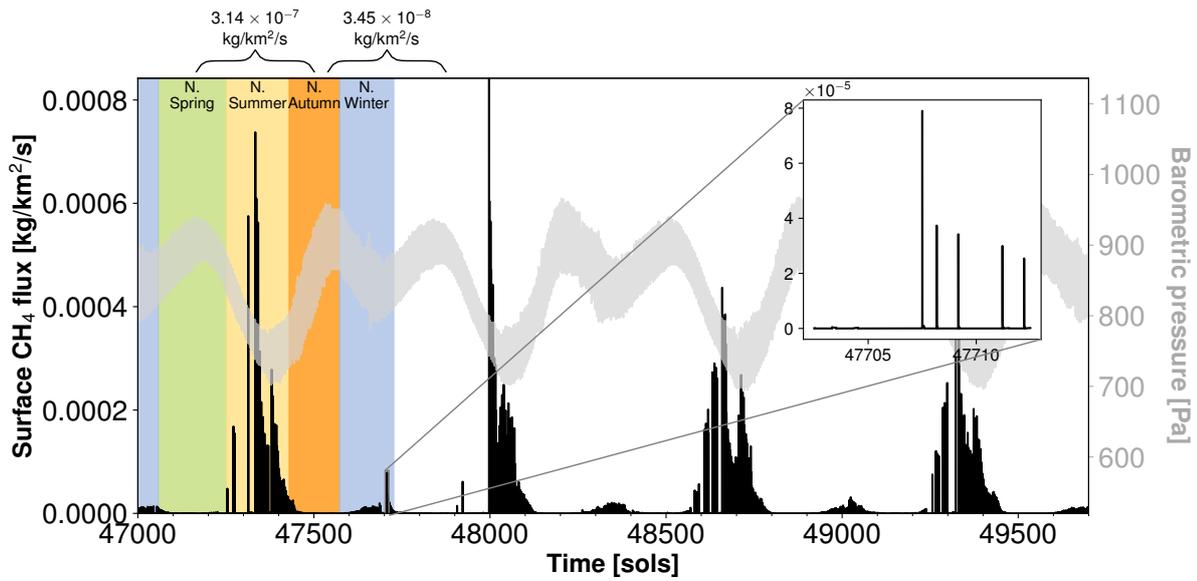


Figure S17. High methane production rate case methane flux (**black**), with barometric pressure forcing (**gray**) driving the subsurface transport model. Hydrogeologic properties are otherwise identical to the base case simulation. Annotations in-figure with curly braces indicate time-averaged fluxes for the 334-sol spans shown, each centered on the local flux maximum. Colored zones indicate Mars seasons for the northern hemisphere. Inset figure highlights the diurnal and semi-diurnal variations in surface methane flux.

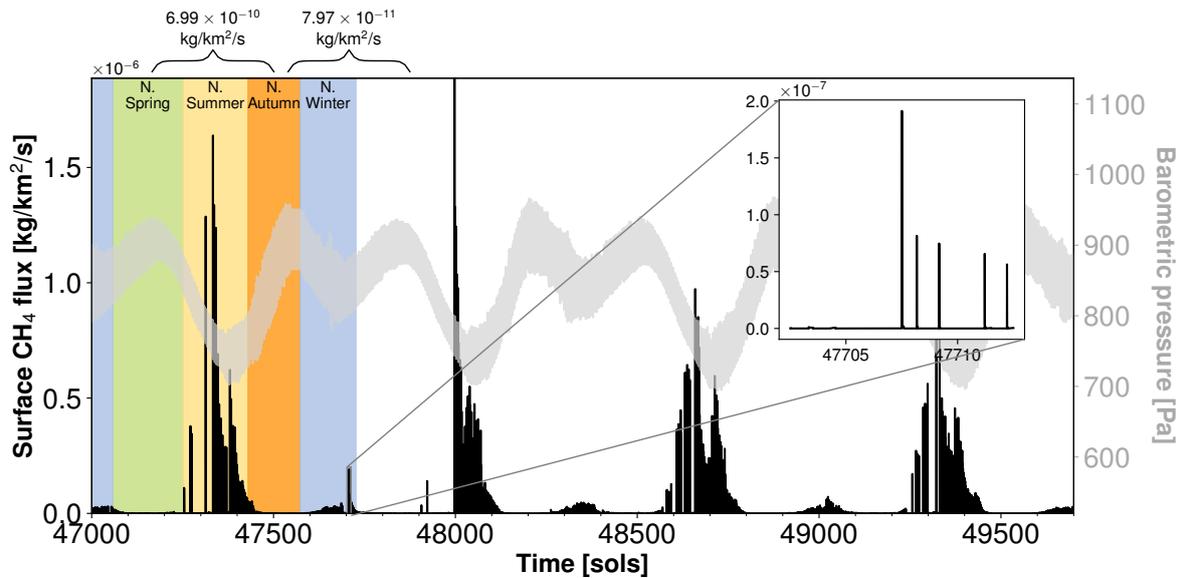


Figure S18. Depth-dependent fracture density case methane flux (**black**), with barometric pressure forcing (gray) driving the subsurface transport model. Hydrogeologic properties are otherwise identical to the base case simulation. Annotations in-figure with curly braces indicate time-averaged fluxes for the 334-sol spans shown, each centered on the local flux maximum. Colored zones indicate Mars seasons for the northern hemisphere. Inset figure highlights the diurnal and semi-diurnal variations in surface methane flux.